

# Physically Parameterized Prediction Equations for Significant Duration in Active Crustal Regions

Kioumars Afshari,<sup>a)</sup> S.M.EERI, and Jonathan P. Stewart,<sup>b)</sup> M.EERI

We develop prediction equations for the median and standard deviation of the significant duration of earthquake ground motions from shallow crustal earthquakes in active tectonic regions. We consider significant duration parameters for 5–75%, 5–95%, and 20–80% of the normalized Arias intensity. The equations were derived from a global database with  $M$  3.0–7.9 events. We find significant noise effects on duration parameters that compel us to exclude some records that had been used previously to develop models for amplitude parameters. Our equations include an  $M$ -dependent source duration term that also depends on focal mechanism. At small  $M$ , the data suggest approximately  $M$ -independent source durations that are close to 1 sec. The increase of source durations with  $M$  is slower over the range  $\sim 5$  to 7.2–7.4 than for larger magnitudes. We adopt an additive path term with breaks in distance scaling at 10 km and 50 km. We include site terms that increase duration for decreasing  $V_{s30}$  and increasing basin depth. Our aleatory variability model captures decreasing between- and within-event standard deviation terms with increasing  $M$ . [DOI: 10.1193/063015EQS106M]

## INTRODUCTION

We develop prediction equations for metrics describing the duration of strong ground motion using a global database for active crustal regions recently developed for the Next Generation Attenuation NGA-West2 project (Ancheta et al. 2014). We utilize functions in which source and path duration are additive (in arithmetic units, i.e., units of sec), consistent with prior work by Abrahamson and Silva (1996) and the second author (Kempton and Stewart 2006; hereafter KS06). For the most part, the present work is an update of KS06 using the much larger NGA-West2 data set, which allows for broadening of the moment magnitude ( $M$ ) and rupture distance ( $R_{rup}$ ) ranges for which the equations are applicable, as well as some adjustments of the equations themselves to capture features of the data.

Prediction equations related to duration parameters published since KS06 include Bommer et al. (2009), Lee and Green (2014), Bora et al. (2014), and Boore and Thompson (2014). None of these studies utilize the large NGA-West2 data set to provide prediction equations for the significant duration parameters most often used for engineering

---

<sup>a)</sup> Graduate Student, UCLA, Civil & Environmental Engineering Dept., Los Angeles, CA, 90095, kafshari@g.ucla.edu

<sup>b)</sup> Professor and Chair, UCLA, Civil & Environmental Engineering Dept., Los Angeles, CA, 90095, jstewart@seas.ucla.edu

applications. In particular, Bommer et al. (2009) utilize the older and smaller NGA-West1 data set (Chiou et al. 2008); Lee and Green (2014) focused principally on duration parameters for stable continental regions, but perform comparative analysis using a small subset of active crustal region data compiled in 2001 (McGuire et al. 2001); Bora et al. (2014) utilize a European data set (Akkar et al. 2014) to develop predictive models for durations computed to optimize the fit of a stochastic ground motion simulation procedure to pseudo spectral accelerations computed from recordings (i.e., the durations are not measured directly from time series); and Boore and Thompson (2014) utilize the NGA-West2 data set, but focus solely on the path term (they do not present source or site terms). Accordingly, the present work fills an important need by providing ground motion prediction equations (GMPEs) for significant duration parameters in active crustal regions using the best data set currently available.

A distinguishing feature of our model relative to other recent duration GMPEs (Bommer et al. 2009, Lee and Green 2014, Bora et al. 2014) is that we take the source and path contributions to duration as additive in arithmetic units (i.e., sec) and the source term is parameterized in physical terms. Other models take source, path, and site terms as additive in natural log units, which is multiplicative in arithmetic units. Source terms are typically linear functions of  $\mathbf{M}$ . We hypothesize that path durations would be better represented as additive to those for source, based on the physics of the problem. In particular, path durations arise in part from the “spreading” of wave arrivals in time due to their different seismic velocities, a process that would be expected to produce path durations that scale approximately with site-to-source distance and to be essentially independent of source duration. We acknowledge that wave scattering provides another physical mechanism that contributes to path duration, and this mechanism is not unambiguously additive to source duration. Ultimately, the selected path function must have compatibility with the data, which we found to support an additive path duration function (described further in the *Path Model* section).

We consider significant duration parameters, which are the most often used duration metrics in engineering applications. Significant duration is defined from the time elapsed between various percentages of Arias intensity, which is computed as:

$$I_A = \frac{\pi}{2g} \int_0^{\infty} [\ddot{u}_g(t)]^2 dt \quad (1)$$

where  $\ddot{u}_g$  is the ground acceleration and  $g$  is acceleration of gravity. Figure 1 shows the accumulation of energy from zero to 100% of  $I_A$  along with times where various percentages are reached. Significant duration parameters considered here are time intervals for 5–75%, 5–95%, and 20–80% of  $I_A$  (denoted  $D_{5-75}$ ,  $D_{5-95}$ , and  $D_{20-80}$ , respectively).

Duration parameters have seen diverse application. The  $D_{5-75}$  and  $D_{5-95}$  parameters have been shown to correlate to collapse capacity of structures (Hancock and Bommer 2007, Raghunandan and Liel 2013, Chandramohan et al. 2016), with increased durations producing reduced capacities. Parameter  $D_{5-95}$  has been used in geotechnical applications including the seismic displacement of landslides (Bray and Rathje 1998). Zhang et al. (2013) have studied the effects of  $D_{5-95}$  and  $D_{15-85}$  on the dynamic response and accumulated damage of

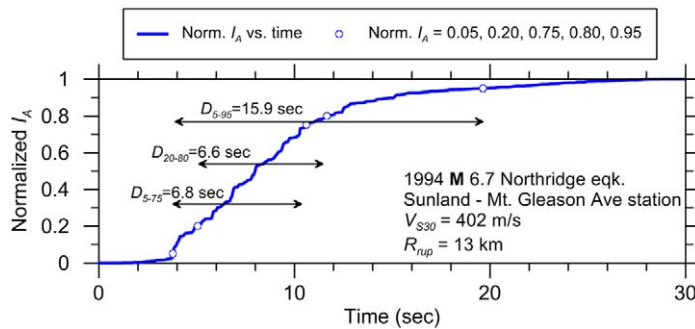


**Figure 1.** Normalized Arias intensity and illustration of three significant duration parameters  $D_{5-75}$ ,  $D_{5-95}$ , and  $D_{20-80}$  for a sample record.

concrete gravity dams. Duration parameters have been shown to correlate to damping scaling factors for horizontal and vertical elastic response spectra, with  $D_{5-75}$  and  $D_{5-95}$  adopted as predictive parameters by [Stafford et al. \(2008\)](#) and  $D_{5-75}$  considered but not adopted by [Rezaeian et al. \(2014a, 2014b\)](#). To our knowledge, parameter  $D_{20-80}$  has not been used in engineering applications, but is considered here because it is less impacted by noisy acceleration signals (details below), and as a result of work by [Boore and Thompson \(2014; hereafter BT14\)](#), who found: (1) it captures the duration of S-wave motions better than other duration metrics by excluding intervals dominated by P-waves and surface waves, and (2) it is strongly correlated to  $D_{5-95}$  in their stochastic simulations ([Boore 2005](#)) as  $D_{5-95} \approx 2D_{20-80}$ .

Subsequent sections of this paper present the prediction equations and regression coefficients. This is followed by descriptions of the manner by which the coefficients were developed, and a review of model performance in terms of residuals analysis and comparisons to prior results in the literature.

## DATA SELECTION

We utilize the NGA-West2 database described by [Ancheta et al. \(2014\)](#). The version of the flatfile that we used in our analysis is dated 29 August 2013 and contains 21,539 pairs of duration parameters for two as-recorded horizontal components. Metadata accompanying each recording that is used in our work includes moment magnitude ( $M$ ), rupture distance ( $R_{rup}$ ), focal mechanism (based on T- and P-axis plunge angles; [Boore et al. 2013](#)), and the  $V_{S30}$  site parameter (time-averaged shear wave velocity in upper 30 m of recording site). Some sites also include the depth to the 1.0 km/s shear wave isosurface ( $z_1$ ).

We initially adopted the data screening protocols of [Boore et al. \(2014; hereafter BSSA14\)](#), some important aspects of which include requiring availability of magnitude, distance, and site metadata, using only data from active crustal regions, excluding records from large structures, and screening of data at large distance as a function of magnitude and instrument type (Figure 1 of BSSA14). We consider ground motions from Class 1 (CL1: main shocks) and Class 2 (CL2: aftershocks) events ([Wooddell and Abrahamson 2014](#)), using

only events having at least four recordings. We exclude any records flagged as questionable by manual inspection by [Ancheta et al. \(2014\)](#); specifically, we require that the “Spectra Quality Flag” under Column JK in the flatfile equals 0. This screening reduced the size of the data set to 11,284 duration pairs.

Records were further screened to remove accelerograms judged to be noise-dominated for a sufficient portion of the record length that much of the energy accumulation is unrelated to seismic wave arrivals. This was a non-trivial process that required considerable data analysis and judgement. To illustrate the issue, Figure 2a shows a record that is noise-dominated in the sense that the normal sequence of wave arrivals is obscured in the accelerogram and high-frequency energy is persistent throughout the recording. Conversely, the record in Figure 2b has clearly evident p- and s-wave arrivals and the frequency content changes across the signal duration. Both records pass screening criteria for GMPEs predicting peak accelerations, velocities, and pseudo-spectral accelerations (such as BSSA14) because spectral ordinates are reliable over some frequency range, whereas we posit that the record in Figure 2a should not be selected for duration GMPE development.

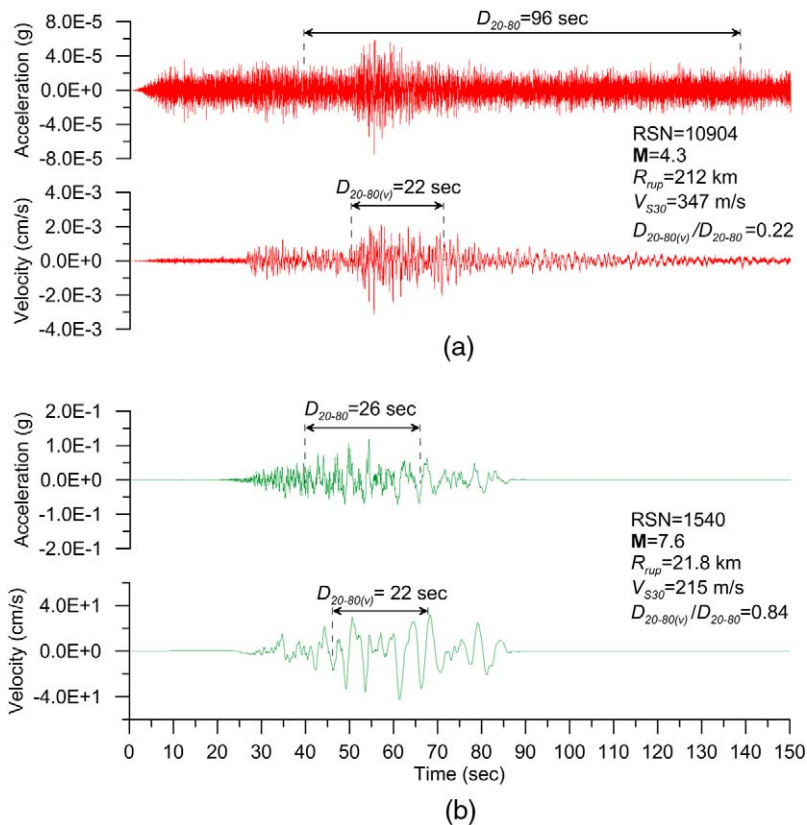


**Figure 2.** Examples of (a) low-amplitude record with duration parameters affected by noise (small value of  $D_{20-80(v)}/D_{20-80}$ ); (b) usable record with duration measures judged as reliable.

The reason for excluding records such as that in Figure 2a is the duration measured from the accelerogram is unreasonably large, reflecting signal noise. While these problems are often obvious from visual inspection, we sought to develop a relatively automated procedure given the large number of records in the NGA-West2 database. A feature we found to often be characteristic of the condition in Figure 2a is that durations measured from velocity time series are much shorter than those from accelerograms [the calculation of significant duration for velocity time series mimics that for acceleration, but with velocity substituted for acceleration in Eq. 1 (similar to Trifunac and Brady, 1975); result is denoted  $D_{20-80(v)}$ ]. For screening purposes, we flag records with  $D_{20-80(v)}/D_{20-80} < 0.65$  for visual inspection, and exclude records which appear to be noisy.

Following application of the above criteria, the data set consists of 22,390 individual-component duration values (11,195 pairs) for each duration parameter. We combine significant durations from the two as-recorded horizontal components to produce 11,195 geometric mean values. Figure 3 shows in red the data distribution in moment magnitude–rupture distance space as well as the subset of data also used by KS06 in blue. Data points shown in grey are those from the NGA-West2 database that did not pass BSSA14 screening criteria, while those in black were excluded by the duration ratio criteria and visual inspection.

## THE EQUATIONS

We formulated equations in consideration of the physical factors described in the *Introduction*, as well as subjective interpretation of nonparametric plots of data such as in Figure 4. Those plots show the magnitude- and distance-dependence of duration for strike-slip earthquakes. The data are adjusted to a uniform site condition of  $V_{S30} = 760$  m/s, using the site model described below (these corrections are small). Important features of the data that are evident from these plots include: the data are insensitive to changes in  $M$  for  $M < \sim 6$ , with modest increases at larger magnitudes; duration increases substantially with distance (i.e., the

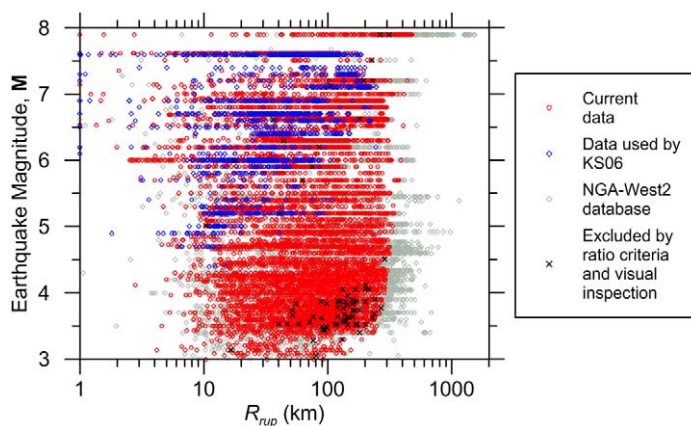


**Figure 3.** Magnitude and distance distribution of data used in the current work and KS06 (records with  $R_{rup} < 1$  km are shown at 1 km). Data points in black were excluded based on the proposed duration ratio criteria and visual inspection.

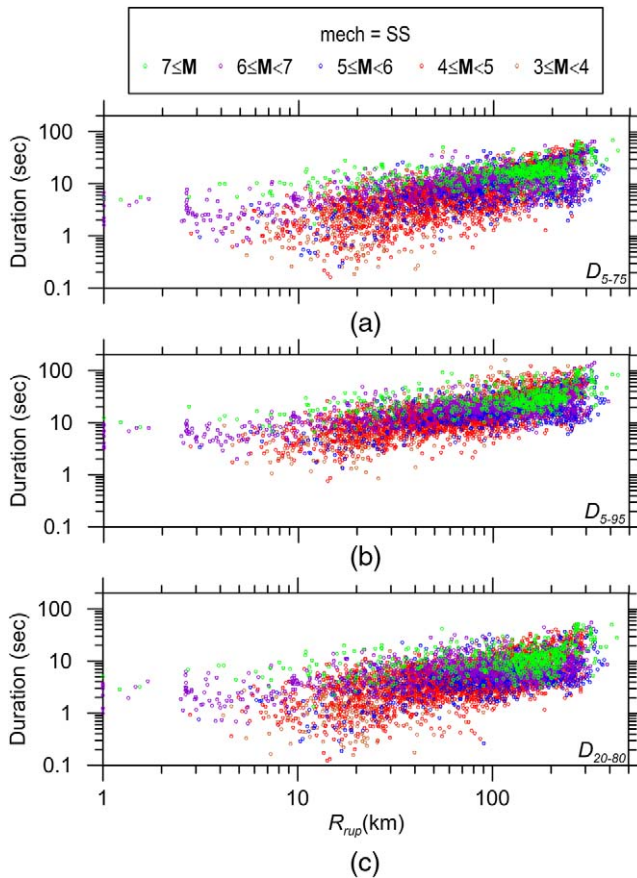


**Figure 4.** Variation with rupture distance of duration parameters for strike-slip earthquakes binned by  $M$ . Records with  $R_{rup} < 1$  km are shown at 1 km.

path duration)—when plotted on log-log axes, the path duration increases with distance in a nonlinear manner, generally becoming progressively steeper with increasing  $R_{rup}$  (this feature is consistent with the notion of path and source durations being additive in arithmetic units, whereas multiplicative models would be linear when plotted in log-log space as in Figure 4); the aforementioned trends with  $M$  and  $R_{rup}$  are consistently observed for the three considered duration parameters; and data dispersion decreases with increasing  $M$  and is smaller for  $D_{5-95}$  than for  $D_{5-75}$  or  $D_{20-80}$ .

We predict ground motion duration using the following expression:

$$\ln D = \ln(F_E(\mathbf{M}, mech) + F_P(R_{rup})) + F_S(V_{S30}, \delta z_1) + \varepsilon_n \sigma(\mathbf{M}) \quad (2)$$

where  $\ln D$  is the natural log of significant duration;  $F_E$  and  $F_P$  are functions for source (“event”) and path durations, respectively, expressed in units of sec;  $F_S$  is a site term that is additive in natural log units (hence multiplicative with the source and path durations);

$\varepsilon_n$  is the standard normal variate representing the fractional number of standard deviations of a single predicted value of  $\ln D$  away from the mean (e.g.,  $\varepsilon_n = -1.5$  is 1.5 standard deviations smaller than the mean); and  $\sigma$  is the total standard deviation of the model. Although not shown here for brevity, the data were found to be log-normally distributed at confidence levels  $>95\%$  (using the Pearson chi-square normality test; [Pearson 1900](#)) when de-trended in the form of residuals.

Source duration is taken as the inverse of the corner frequency ( $f_c$ ) in the Fourier Amplitude Spectrum ([Hanks and McGuire 1981](#)):

$$F_E = \begin{cases} 1/f_0 & \mathbf{M} > \mathbf{M}_1 \\ b_0(\text{mech}) & \mathbf{M} \leq \mathbf{M}_1 \end{cases} \quad (3)$$

The use of a constant duration ( $b_0$ ) at small magnitudes ( $\mathbf{M} \leq \mathbf{M}_1$ ) is motivated by the lack of  $\mathbf{M}$ -dependence in the data for small magnitudes, as shown in Figure 4. Corner frequency is related to seismic moment and stress drop as ([Brune 1970, 1971](#)):

$$f_0 = 4.9 \cdot 10^6 \beta (\Delta\sigma/M_0)^{1/3} \quad (4)$$

where  $\beta$  is the shear wave velocity at the source (taken as 3.2 km/s),  $\Delta\sigma$  is stress parameter in bars (following KS06, we interpret  $\Delta\sigma$  as an index parameter loosely related to stress drop for model-building purposes), and  $M_0$  is the seismic moment in dyne-cm, which is computed as ([Hanks and Kanamori 1979](#)):

$$M_0 = 10^{1.5\mathbf{M}+16.05} \quad (5)$$

Stress index parameter  $\Delta\sigma$  as used here is intended to capture source duration characteristics only, and as such, should not be confused with terms such as *stress drop* or *stress parameter* used elsewhere in studies of ground motion amplitude (e.g., [Atkinson and Beresnev 1997](#), [Boore 2003](#)). We relate  $\Delta\sigma$  to  $\mathbf{M}$  using two connected line segments:

$$\Delta\sigma = \begin{cases} \exp[b_1(\text{mech}) + b_2(\mathbf{M} - \mathbf{M}^*)] & \mathbf{M} \leq \mathbf{M}_2 \\ \exp[b_1(\text{mech}) + b_2(\mathbf{M}_2 - \mathbf{M}^*) + b_3(\mathbf{M} - \mathbf{M}_2)] & \mathbf{M} > \mathbf{M}_2 \end{cases} \quad (6)$$

where  $b_1$ ,  $b_2$ ,  $b_3$ , and  $\mathbf{M}_2$  are model parameters and  $\mathbf{M}^*$  is a reference magnitude (taken as 6).

Path duration is linearly dependent on distance  $R_{rup}$ , but with different slopes for three  $R_{rup}$  intervals with changing slopes at  $R_1$  and  $R_2$ :

$$F_P = \begin{cases} c_1 R_{rup} & R_{rup} \leq R_1 \\ c_1 R_1 + (c_2)(R_{rup} - R_1) & R_1 < R_{rup} \leq R_2 \\ c_1 R_1 + (c_2)(R_2 - R_1) + (c_3)(R_{rup} - R_2) & R_{rup} > R_2 \end{cases} \quad (7)$$

where  $c_1$  to  $c_3$ ,  $R_1$  and  $R_2$  are model parameters. Site term  $F_S$  is taken as:

$$F_S = \begin{cases} c_4 \ln\left(\frac{V_{S30}}{V_{ref}}\right) + F_{\delta z_1} & V_{S30} \leq V_1 \\ c_4 \ln\left(\frac{V_1}{V_{ref}}\right) + F_{\delta z_1} & V_{S30} > V_1 \end{cases} \quad (8)$$



$$F_{\delta z_1} = \begin{cases} c_5 \delta z_1 & \delta z_1 \leq \delta z_{1,ref} \\ c_5 \delta z_{1,ref} & \delta z_1 > \delta z_{1,ref} \end{cases} \quad (9)$$

Parameters  $c_4$ ,  $c_5$ ,  $V_{ref}$ ,  $V_1$ , and  $\delta z_{1,ref}$  are model parameters set by regression or by visual inspection of the data. The model produces scaling with  $V_{S30}$  only for  $V_{S30} \leq V_1$ . The basin depth term  $F_{\delta z_1}$  captures the effects of depth to bedrock which is dependent on sediment depth differential  $\delta z_1$ . The scaling is present for  $\delta z_1$  smaller than the upper limit  $\delta z_{1,ref}$ . According to BSSA14,  $\delta z_1$  is calculated as the difference between the depth to shear wave velocity of 1,000 m/s for the site ( $z_1$ ), and a median depth  $\mu_{z1}$  conditional on  $V_{S30}$ :

$$\delta z_1 = z_1 - \mu_{z1}(V_{S30}) \quad (10)$$

Depth  $z_1$  is best obtained from a site-specific  $V_S$  profile that penetrates the 1,000 m/s shear-wave horizon. Lacking that information,  $z_1$  can be estimated using basin models in the literature, which are currently available for Japan and urban portions of California (links and references given in Seyhan et al. 2014) as well as Seattle (Frankel et al. 2007) and Taipei, Taiwan (Wang et al. 2004). Median depth  $\mu_{z1}$  conditional on  $V_{S30}$  can be computed for California and Japan as:

$$\text{California: } \ln(\mu_{z1}) = \frac{-7.15}{4} \ln\left(\frac{V_{S30}^4 + 570.94^4}{1360^4 + 570.94^4}\right) - \ln(1000) \quad (11)$$

$$\text{Japan: } \ln(\mu_{z1}) = \frac{-5.23}{2} \ln\left(\frac{V_{S30}^2 + 412.39^2}{1360^2 + 412.39^2}\right) - \ln(1000) \quad (12)$$

where  $\mu_{z1}$  is in units of km and  $V_{S30}$  is in units of m/sec. Models for  $\mu_{z1}$  are not currently available outside of California and Japan; such applications should use a default value of  $\delta z_1 = 0$ .

The total standard deviation  $\sigma$  is partitioned into components representing between- and within-event standard deviations ( $\tau$  and  $\phi$ , respectively):

$$\sigma(\mathbf{M}) = \sqrt{\tau^2(\mathbf{M}) + \phi^2(\mathbf{M})} \quad (13)$$

The  $\mathbf{M}$ -dependent component standard deviations are given by:

$$\tau(\mathbf{M}) = \begin{cases} \tau_1 & \mathbf{M} < 6.5 \\ \tau_1 + (\tau_2 - \tau_1) \left( \frac{\mathbf{M} - 6.5}{7 - 6.5} \right) & 6.5 \leq \mathbf{M} < 7 \\ \tau_2 & \mathbf{M} \geq 7 \end{cases} \quad (14)$$

$$\phi(\mathbf{M}) = \begin{cases} \phi_1 & \mathbf{M} < 5.5 \\ \phi_1 + (\phi_2 - \phi_1) \left( \frac{\mathbf{M} - 5.5}{5.75 - 5.5} \right) & 5.5 \leq \mathbf{M} < 5.75 \\ \phi_2 & \mathbf{M} \geq 5.75 \end{cases} \quad (15)$$

where parameters  $\tau_1$ ,  $\tau_2$ ,  $\phi_1$ , and  $\phi_2$  are estimated based on values of  $\mathbf{M}$ -dependent  $\tau$  and  $\phi$ . Model coefficients are given in Tables 1–3.



**Table 1.** List of parameters used for source model (N: normal, R: reverse, SS: strike-slip)

	$M_1$	$M_2$	$M^*$	$b_0$ (sec)	$b_1$	$b_2$	$b_3$
$D_{5-75}$	5.35	7.15	6	1.555 (N) 0.7806 (R) 1.279 (SS) 1.280 (Unknown)	4.992 (N) 7.061 (R) 5.578 (SS) 5.576 (Unknown)	0.9011	-1.684
$D_{5-95}$	5.2	7.4	6	2.541 (N) 1.612 (R) 2.302 (SS) 2.182 (Unknown)	3.170 (N) 4.536 (R) 3.467 (SS) 3.628 (Unknown)	0.9443	-3.911
$D_{20-80}$	5.2	7.4	6	1.409 (N) 0.7729 (R) 0.8804 (SS) 0.8822 (Unknown)	4.778 (N) 6.579 (R) 6.188 (SS) 6.182 (Unknown)	0.7414	-3.164

**Table 2.** List of parameters used for the path model and site terms

	$c_1$ (sec/km)	$c_2$ (sec/km)	$c_3$ (sec/km)	$c_4$ -	$c_5$ (1/km)	$R_1$ (km)	$R_2$ (km)	$V_1$ (m/s)	$V_{ref}$ (m/s)	$\delta z_{1,ref}$ (m)
$D_{5-75}$	0.1159	0.1065	0.0682	-0.2246	0.0006	10	50	600	368.2	200
$D_{5-95}$	0.3165	0.2539	0.0932	-0.3183	0.0006	10	50	600	369.9	200
$D_{20-80}$	0.0646	0.0865	0.0373	-0.4237	0.0005	10	50	600	369.6	200

**Table 3.** List of parameters used for standard deviation components

	$\tau_1$	$\tau_2$	$\phi_1$	$\phi_2$
$D_{5-75}$	0.28	0.25	0.54	0.41
$D_{5-95}$	0.25	0.19	0.43	0.35
$D_{20-80}$	0.30	0.19	0.56	0.45

# MODEL DEVELOPMENT

Our GMPEs were developed in a phased process in which certain model elements were held constant (e.g., path and site) while one was regressed against the data (e.g., source). The subsequent phase would then hold the just-established model element fixed while regressing another component. Phasing of this sort was required because a single mixed-effects

regression with the full function would not converge. We describe the specific implementation of this approach for the source, path, and site terms in the following sections.

PRIMARY SOURCE MODEL: M-SCALING

The source model consists of constant term  $b_0$  for  $M < M_1$  and  $M$ -dependent terms at larger magnitudes. Per Equations 4–6, a source model in which duration is constant with respect to  $M$  requires linear scaling of  $\Delta\sigma$  with  $M$  at a slope of  $b_2 = b_3 = 3.45$ . This slope is shown in Figure 5 with a dashed blue line. The steep increase of  $\Delta\sigma$  with  $M$  shown by this line is required to keep  $f_0$  high and duration low as  $M$  increases.

We regress the duration data to investigate the variation of  $\Delta\sigma$  with  $M$ , expecting slower scaling of  $\Delta\sigma$  than required for the constant duration model. In the first phase of this regression, we adopted the function in Equations 2–6 but with no site term ( $F_S = 0$ ), path coefficient  $c_1$  in Equation 7 set from KS06 ( $c_2$  and  $c_3$  were taken as zero for this preliminary analysis), and  $\Delta\sigma$  as a free parameter. We evaluated source duration for each individual earthquake using mixed-effects regression performed with the LME routine in program R (Pinheiro et al. 2013). The estimated source duration is then converted to  $\Delta\sigma$  using Equations 3–4, with results similar to those shown by the discrete symbols in Figure 5. Using this same process, we also evaluate median values of  $\Delta\sigma$  for events within bins 0.5 magnitude units in width using mixed effects procedures (marked as “binned medians” in Figure 5).

The discrete data points and binned medians shown in Figure 5 were derived following several phases of analysis in which source and path terms were incrementally adjusted (details below). The plotted points reflect the  $\Delta\sigma$  values that are derived when the final recommended path and site terms are considered in the derivation of the event-specific stress drop indices  $\Delta\sigma$ . The results in Figure 5 are for the  $D_{20-80}$  duration parameter—similar results for the other duration parameters are given in the Electronic Supplement.

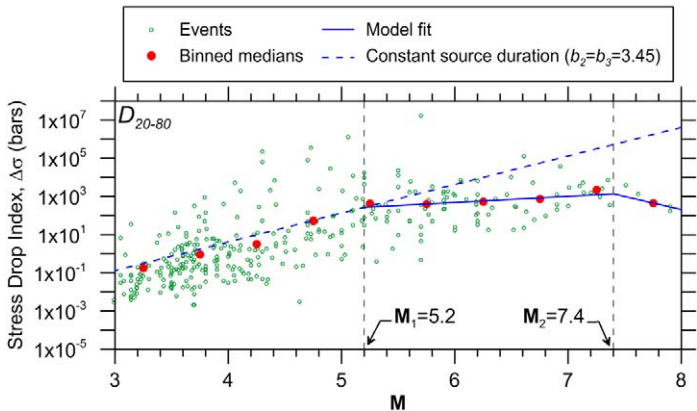


**Figure 5.** Stress drop index values calculated for each event for the  $D_{20-80}$  duration measure, as well as the binned medians and fitted function (mechanism-independent).

Source durations for some earthquakes do not appear in Figure 5; this occurs when source durations (obtained from the subtraction of path durations from observations) are negative, in which case  $\Delta\sigma$  is undefined for that event. In contrast, the binned median values of  $\Delta\sigma$  are computed using all events within the bin, including those producing a negative source duration. This can cause the binned median values of  $\Delta\sigma$  in Figure 5 to not plot near the center of the data (this occurs near  $M_1$  for  $D_{20-80}$  and  $D_{5-95}$ , see Figures 5 and A1b).

The trends of the results in Figure 5 indicate that  $\Delta\sigma$  increases with  $M$  at progressively slower rates as  $M$  increases across the considered range of  $M = 3 - 8$ . We parsed the full range into three intervals bounded by  $M_1$  (at about 5–5.5) and  $M_2$  (at about 7–7.5). For  $M < M_1$ ,  $\Delta\sigma$  increases with  $M$  at approximately the rate required for  $M$ -independent source duration for  $D_{20-80}$ , and at even faster rates for other duration parameters (Figure A1). We consider this feature of the computed stress drop indices to be influenced by difficulties in properly separating path from source durations for small  $M$  events, where source durations are small and noise effects in the data are large. Nonetheless, the data in Figure 5 support the  $M$ -independent model represented by coefficient  $b_0$  in Equation 3, which is the source duration at  $M = M_1$  in units of seconds. As such, our model can be used to provide duration predictions for  $M < M_1$ , albeit with a higher degree of epistemic uncertainty than at higher magnitudes. We recognize that this  $M$ -independent duration feature of the low-magnitude data requires the stress drop term to exhibit stronger magnitude-dependence than has been observed previously for amplitude-related ground motion intensity measures (Allmann and Shearer 2007, 2009). This presumably occurs because source attributes affecting low-frequency ground motions (i.e., near corner frequency,  $f_0$ ) are not perfectly correlated with those controlling duration, at least with respect to their relative magnitude-dependencies. We accept these differences in  $\Delta\sigma$  trends because our objective is to capture features of duration data. This underscores our previous remark that  $\Delta\sigma$  is a stress index and should not be confused with other stress parameters in the literature used for prediction of ground motion amplitude.

For  $M > M_1$ ,  $\Delta\sigma$  increases with  $M$  at a slower rate that required for a constant duration model, indicating that source duration increases with  $M$  as expected. For the two largest events in the NGA-West2 data set ( $M$  7.9 Denali, Alaska, and  $M$  7.9 Wenchuan, China),  $\Delta\sigma$  is markedly lower than suggested by a trend line established at lower magnitudes. We considered ignoring these features and simply extending the linear relation between  $\Delta\sigma$  and  $M$  beyond  $M_2$ . However, such an approach produces severe distortion of residuals at large magnitudes, and so we elected to capture this feature of the data in our model. We acknowledge that other modelers may make different decisions in this regard, and as such, that model performance at large magnitudes ( $M > M_1$ ) is subject to larger epistemic uncertainty than at lower  $M$ . We considered alternate functions to capture this feature of the data (bilinear with second line being flat, parabolic), but after much trial and error settled upon the trilinear model shown in Figure 5 that allows  $\Delta\sigma$  to have a negative slope set by data at large magnitudes ( $M > M_2$ ). The model fit shown in Figure 5 for  $M > M_1$  is based on a simple least-squares linear regression through the binned medians to set coefficients  $b_1 - b_3$ . Attempts to set these coefficients through alternative procedures (linear mixed effects regression and least-squares linear regression through event-specific  $\Delta\sigma$  values) produced poorer fits to the data than the adopted approach.

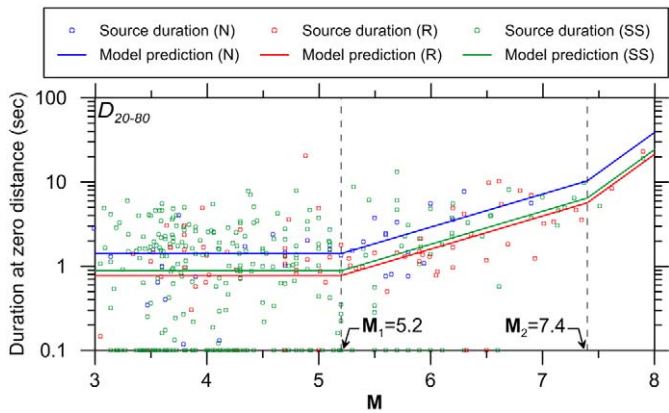


**Figure 6.** Average source durations for  $D_{20-80}$  by event type, evaluated from stress drop index per Equations 3 and 4. Source durations smaller than 0.1 sec are plotted at 0.1 sec.

Focal mechanism affects the low- $M$  duration ( $b_0$ ) and the apparent stress drop scaling term  $b_1$ . We initially estimated those parameters as overall averages set by regression without consideration of mechanism. Those values are given in Table 1 with the mechanism marked as “unknown.” The adjustments for focal mechanism were then set following establishment of path scaling through residuals analysis, as described further in the *Secondary Effects* section below. Results of those analyses are reflected in the mechanism-dependent  $b_0$  and  $b_1$  coefficients in Table 1 and are illustrated in Figure 6. Normal fault earthquakes have the largest source durations for a given  $M$  and reverse mechanisms the smallest, with strike-slip being intermediate. Also shown in Figure 6 are event-specific source durations compatible with their associated stress drop indices (from Figure 5).

Because of the aforementioned difficulties in separating source and path durations for low magnitude data (i.e., for events with  $M < M_1$ ), work on other model components (other than primary magnitude-scaling) utilized data with  $M \geq M_1$ . This smaller subset of data consists of 5,903 recordings from 107 earthquakes for  $D_{5-75}$ , and 6,089 recordings from 114 earthquakes for  $D_{5-95}$  and  $D_{20-80}$ . The applicability of path and site models developed on this basis for lower magnitudes is verified subsequently through residuals analysis.

**PATH MODEL**

The path model consists of distance scaling coefficients  $c_1$  to  $c_3$ , which differentiate path scaling rates for three distance ranges:  $R_{rup} \leq R_1$ ,  $R_1 < R_{rup} \leq R_2$ , and  $R_{rup} > R_2$ . As indicated in the *Introduction*, our path term is additive with source duration, which is different from most recent duration GMPEs but consistent with KS06 and BT14. KS06 used a simple linear path scaling function, whereas BT14 use a multi-linear function with slope breaks at 7 km, 45 km, 125 km, 175 km, and 270 km.

As described in the previous section, our first iteration in developing the source model regressed for parameters  $b_1 - b_3$  with path terms fixed at the values from KS06. In order to guide our selection of a path function, we then sought to “turn off” the path model and

identify misfits of the data relative to a path-removed model with adjustments for event-specific data/model misfits. This was done by first computing residuals between data and model:

$$R_{ij} = \ln D_{ij} - \mu_{ij}(\mathbf{M}, R_{rup}) \quad (16)$$

where  $\mu_{ij}$  is the GMPE mean in natural log units for recording  $j$  in event  $i$ . Those residuals were then partitioned into between- and within-event components as follows using mixed-effects analysis as implemented in the LME command in program R (Pinheiro et al. 2013):

$$R_{ij} = c_k + \eta_i + \varepsilon_{ij} \quad (17)$$

In this approach,  $c_k$  is the overall model bias (nearly zero since residuals are being computed for the same data used in model development),  $\eta_i$  is the between-event residual (event term) for earthquake  $i$ , which represents the degree to which an individual event is high or low relative to the average, and  $\varepsilon_{ij}$  is the within-event residuals for recording  $j$  in event  $i$ .

Armed with  $\eta_i$  values, we then computed record-specific path duration against an approximately bias-removed source model as follows:

$$F_{P,ij} = D_{ij} - \exp[\mu_{ij}^0(\mathbf{M}, R_{rup} = 0) + \eta_i] \quad (18)$$

where the superscript “0” on  $\mu_{ij}^0$  is to indicate that the duration prediction has the path term removed (equivalent to setting  $R_{rup} = 0$ ). We plot in Figure 7 the quantity  $F_{P,ij}$  (in units of sec) against  $R_{rup}$  for the  $D_{20-80}$  duration parameter. We found this form for the plots to be useful in guiding selection of a path duration function. The data points shown in Figure 7 are derived from the final model, following multiple iterations whereby in each iteration the path model is modified, and those modified path models are used to re-derive the source model. Through this process the trends of the path terms were relatively consistent from iteration-to-iteration. Moreover, whereas initial stages of this analysis did not consider site effects in the

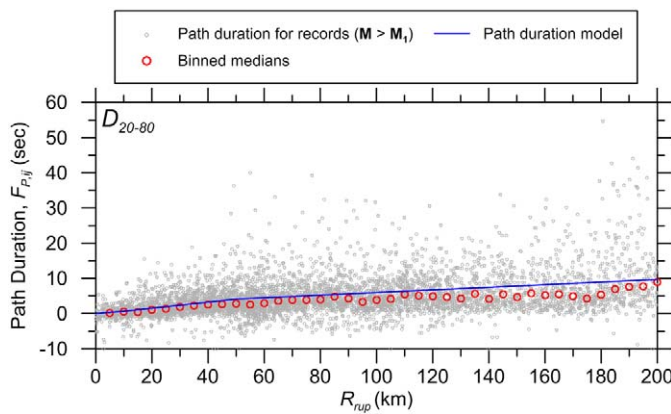


**Figure 7.** Path durations calculated for  $D_{20-80}$ ; path duration points calculated for records with  $M > M_1$  after subtracting the source duration and the effects of event-to-event variability ( $\eta_i$ ). Binned medians also shown along with model fit.

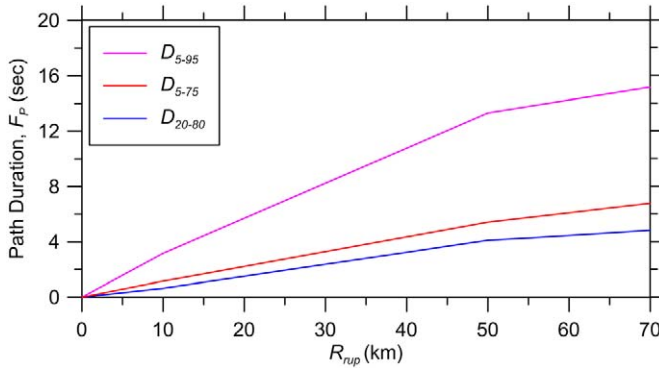


**Figure 8.** Mean path durations predicted for the three duration measures.

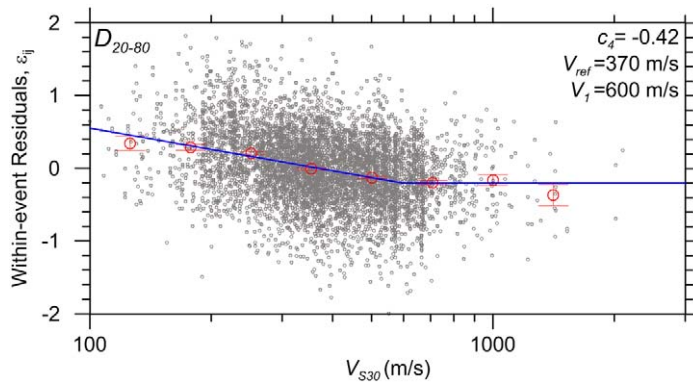
derivation of  $F_{P,ij}$ , in the final iteration site effects were included in the analysis of  $\mu_{ij}^0$  in Equation 18.

Figure 7 shows individual  $D_{20-80}$  path durations for  $\mathbf{M} > \mathbf{M}_1$  along with median values within equally spaced distance bins. The most clearly evident data trends in Figure 7 are relatively linear above and below a transition distance of 50 km, with faster path scaling at closer distances. When the data was fit in this manner, we encountered misfit for  $R_{rup} < 10$  km, so a second break in the path term was introduced at 10 km. Coefficients for the resulting tri-linear distribution were derived from nonlinear least squares regression as part of the iterative model derivation [the use of least squares in this case is compatible with the principles of mixed effects regression, because random effects (event terms) have been removed from each data point]. The resulting fit to data is shown in Figure 7. The model fit is slightly higher than the binned medians because model coefficients are set to fit the mean of the data. Trends similar to those shown in Figure 7 were found for duration parameters  $D_{5-75}$  and  $D_{5-95}$  as well, as shown in Figure A3 in the appendix. Figure 8 shows that path durations are ordered as  $D_{20-80} < D_{5-75} < D_{5-95}$  (total durations typically order as  $D_{20-80} \sim D_{5-75} < D_{5-95}$ ; Figure 8 shows model fits only).

We queried the path durations for possible  $\mathbf{M}$ -dependency. When the path durations are separated into distinct  $\mathbf{M}$  bins, F-tests (Cook and Weisberg 1999) do not show the results to be significantly distinct. The finding that path durations are not significantly different over the wide  $\mathbf{M}$  range in the data set indicates that an additive path function is preferred to a multiplicative function, which would necessarily couple path duration with magnitude. We note that BT14 also recommend an  $\mathbf{M}$ -independent path duration.

### PRIMARY SITE MODEL: $V_{S30}$ -SCALING

Our model development process reached stable and consistent results for the source and path models by performing multiple iterations in which these model components were successively regressed using the function in Equation 2 with the site term  $F_S$  set to zero. We then examined site effects using mixed effects residuals analysis (Equations 16–17) with records from events with  $\mathbf{M} > \mathbf{M}_1$ . We investigated  $V_{S30}$ -scaling by plotting within-event residuals



**Figure 9.**  $V_{S30}$ -dependence of within-event residuals of model in which site term  $F_S$  in Equation 2 is set to zero for  $D_{20-80}$ . Individual data points are shown for records with  $M > M_1$  along with binned means, their 95% confidence intervals, and the final fit. The final model uses the slope ( $c_4$ ) and limiting velocity ( $V_l$ ) marked in the figure.

( $\epsilon_{ij}$  from Equation 17) against  $V_{S30}$  as shown in Figure 9 for  $D_{20-80}$  (similar results are in Figure A4 for other duration metrics). The figure shows individual data points, binned means, and the fit line as described further below.

We find the binned means of residuals to decrease essentially linearly with  $V_{S30}$  up to a limiting value ( $V_l$ ) of 600 m/s. The slopes are modest, being approximately  $-0.22$ ,  $-0.32$ , and  $-0.42$  for  $D_{5-75}$ ,  $D_{5-95}$ ,  $D_{20-80}$ , respectively. For comparison,  $V_{S30}$ -gradients for PGA and PGV are approximately  $-0.6$  and  $-0.84$ , respectively (Seyhan and Stewart 2014). The trends shown in Figure 9 motivated selection of the  $V_{S30}$ -scaling function in Equation 8. The regression results are indicated in Table 2.

Final coefficients for the site model were obtained using an iterative process in which the fit through the binned means is added to the site term from previous step until reaching a flat trend in  $\epsilon_{ij}$  against  $V_{S30}$  at the final iteration. Once the site model had been established in this manner, site corrections were applied in the development of the final source and path durations and related regressions, with the results presented in prior sections.

## SECONDARY EFFECTS

Once the primary  $M$ -scaling function (using the mechanism-independent  $b_0$  and  $b_1$  values), path function, and  $V_{S30}$ -scaling had been established, we investigated additional effects related to focal mechanism, event type, and basin depth through mixed-effects residuals analysis carried out using Equations 16–17.

The effects of focal mechanism are investigated by binning event terms  $\eta_i$  by event type for  $M > M_1$ , as shown in Figure 10 along with binned means. Relative to a mechanism-independent model, we find strike-slip earthquakes to be effectively unbiased (unsurprising as they dominate the data set) and normal- and reverse-slip events to have positive and negative bias, respectively. These trends for duration are opposite to those for high-frequency pseudo-spectral accelerations (high amplitudes are associated with short durations and



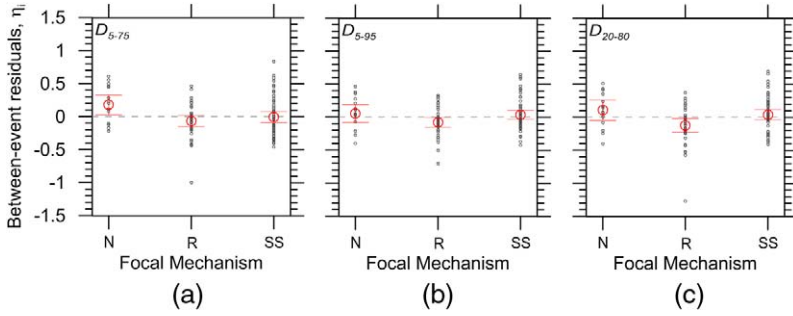


**Figure 10.** Between-event residuals binned by focal mechanism for records with  $M > M_1$  along with binned means and their 95% confidence intervals indicating the systematic biases for different focal mechanisms. Results shown for all three investigated duration parameters.

vice-versa), which is consistent with prior work showing negative correlation between these ground motion intensity measures (Bradley 2011). The mean values for the respective bins guided the mechanism-specific  $b_0$  and  $b_1$  values in Table 1.

In Figure 11a, we show event terms for CL1 and CL2 event types against  $M$ . The regions contributing the majority of the CL2 data are China and California. The CL2 events from China are generally in the range  $M \sim 4.5$ -6 and have negative event terms. Similar trends for Chinese CL2 events, but with positive event terms, were found by Boore et al. (2013) for some amplitude-related intensity measures. While casual inspection of Figure 11a suggests the presence of  $M$  ranges with significant bias of CL2 events relative to CL1 events, an evaluation of this type fails to account for several key features of the data: (1) of the 104 CL2 events, 49 are from a single event (Wenchuan) and 14 are single CL2 events trailing a main shock CL1 event. Hence, the data sampling (in terms of numbers of CL2 events following the parent CL1 events) is highly non-uniform.

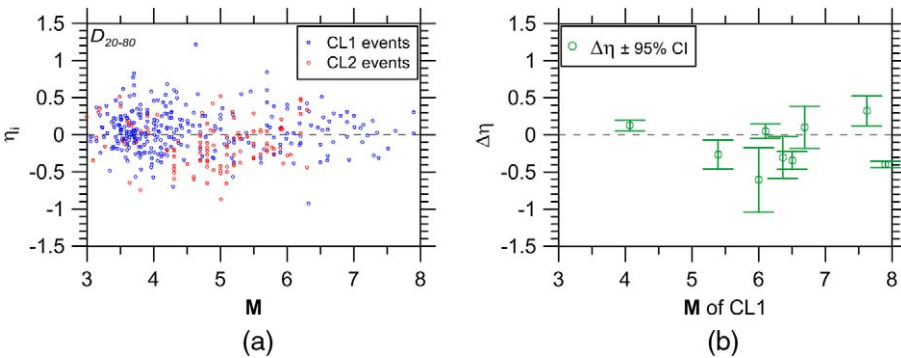


**Figure 11.** (a) Between-event  $D_{20-80}$  residuals plotted against  $M$  for CL1 and CL2 events, and (b) differential event terms ( $\Delta\eta$ ) plotted against the magnitude of their parent event along with 95% confidence intervals.

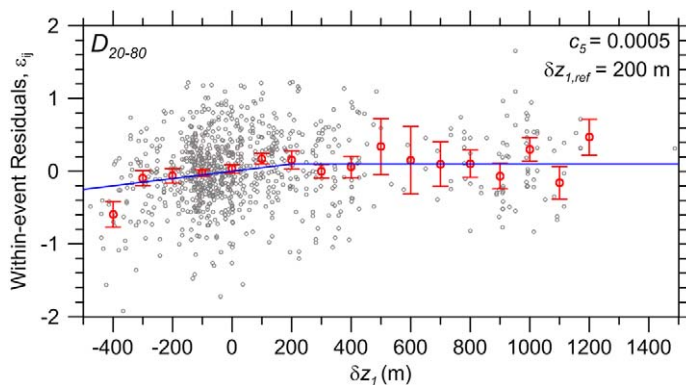


**Figure 12.** Variation of within-event residuals with basin depth differential  $\delta z_1$  for  $D_{20-80}$  using records with  $\mathbf{M} > \mathbf{M}_1$ . The plotted residuals were derived without using a basin depth term in the site model.

As was done for amplitude by BSSA14 and Boore et al. (2013), we consider the differences between CL2 events and the parent CL1 event to be a more robust means by which to assess the effects of event type, because it accounts for possible correlations between parent and child event terms. We consider CL1 events with 3 or more child CL2 events. For each pairing, we compute  $(\Delta\eta = \bar{\eta}_{C2} - \eta_{C1})$ , where  $\bar{\eta}_{C2}$  is the mean of the CL2 event terms and  $\eta_{C1}$  is the event term for the parent CL1 event. Figure 11(b) shows the resulting values of  $\Delta\eta$  as a function of  $\mathbf{M}$  for the CL1 event. We see no significant trend in the results, nor any particular bias. Accordingly, we conclude that the GMPEs, which were developed using both CL1 and CL2 events, can be considered applicable to both. Plots similar to Figure 11 for other duration parameters are shown in Figures A5 and A6 in online Appendix A.

As shown in Figure 12, the effects of basin depth were investigated by plotting within-event residuals for  $\mathbf{M} > \mathbf{M}_1$  against basin depth differential  $\delta z_1$  for the subset of the data where this parameter is available. We find no scaling with  $\delta z_1$  for  $\delta z_1 > 200$  m; note this does not imply no dependence of duration on depth in this range, but merely indicates that information on basin depth does not carry predictive power beyond the default basin depths associated with  $V_{S30}$ . For  $\delta z_1 < \sim 200$  m, residuals increase with  $\delta z_1$  in a statistically significant manner (based on non-overlapping confidence intervals of binned means at the limits of the range). A two-segment linear function was fit through the binned means to establish the coefficients in Equation 9.

## MODEL PERFORMANCE

### RESIDUALS

The performance of the final model, following the many adjustments and iterations described in the prior sections, is tested by mixed-effects residuals analysis (Equations 16 and 17). These residuals analyses are performed both for the subset of data with  $\mathbf{M} > \mathbf{M}_1$

(encompassing most engineering applications) and for the full data set including smaller magnitudes.

For the  $M > M_1$  data, overall model bias term  $c_k$  is 0.0099,  $-0.0002$ , and  $0.0393$  for parameters  $D_{5-75}$ ,  $D_{5-95}$ , and  $D_{20-80}$ , respectively. These are considered acceptably small. Plots of between-event residuals ( $\eta_i$ ) and within-event residuals ( $\varepsilon_{ij}$ ) against relevant independent variables are shown in Figure 13 for  $D_{20-80}$ ; similar plots for other duration parameters are in the appendix (Figures A8–A9). Performance of the source model is judged by plots of  $\eta_i$  versus  $M$  and by binned means within focal mechanism groups. As shown in Figure 13, these trends are flat for  $M > M_1$ . Performance of the path and site models is judged from trends of  $\varepsilon_{ij}$  against rupture distance  $R_{rup}$  and  $V_{S30}$ , respectively. The trends are flat, suggesting these effects are properly captured in the model. The data for  $R_{rup} < \sim 3$  km are sparse, so we have less confidence in the robustness of the trends in this range. Although not shown in Figure 13, there are also no trends with  $\delta z_1$ .

Residuals analyses were also performed for the full data set. The model exhibits some bias relative to this data, which we illustrate by plotting the sum  $c_k + \eta_i$  against  $M$  in Figure 14a. The bias occurs for  $M < M_1$  events, being negative near  $M_5$  and positive

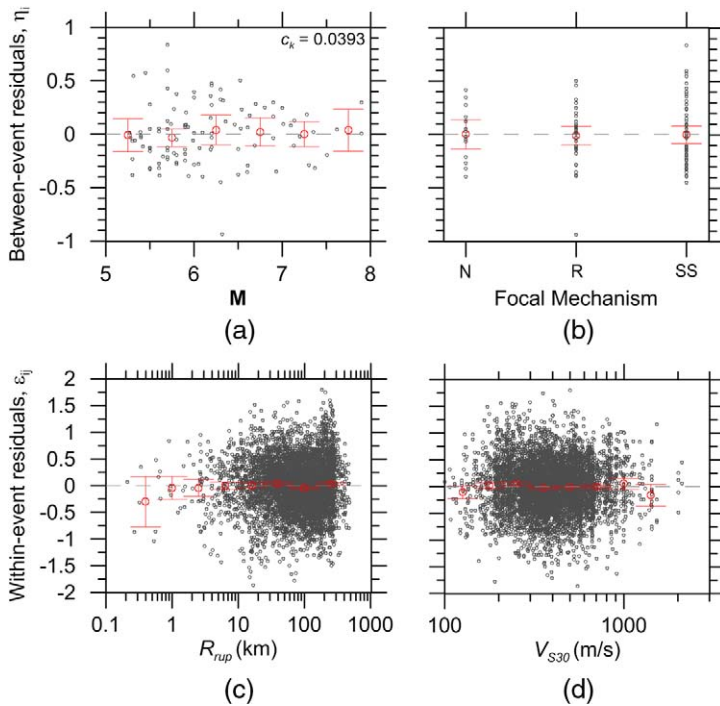


**Figure 13.** Plots of between-event and within-event residuals for  $D_{20-80}$  along with their binned means and 95% confidence intervals showing their trends with (a) magnitude, (b) focal mechanism, (c) distance, and (d)  $V_{S30}$ .

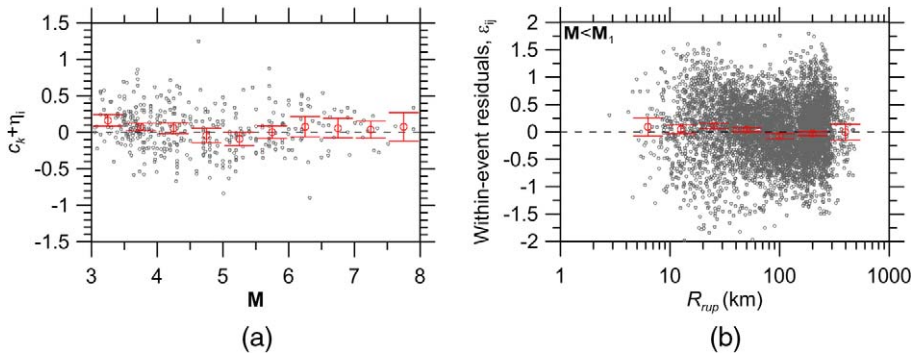


**Figure 14.** Plots of between-event and within-event residuals for  $D_{20-80}$  along with their binned means and 95% confidence intervals showing trends with (a) magnitude, using data across the full  $M$  range, and (b) rupture distance, using data for  $M < M_1$  only.

for  $M < \sim 4.5$ . We consider these source duration trends from the data to be unrealistic and to reflect aforementioned difficulties in separating source and path effects at small magnitudes. For this reason, we did not attempt to model these features, instead adopting a relatively simple  $M$ -independent source duration for  $M < M_1$ . Figure 14b shows trends of  $\varepsilon_{ij}$  with distance for the  $M < M_1$  data only. The binned means of these residuals retain a nearly flat trend with distance, with the 95% confidence interval for most bins encompassing zero. This indicates that the path durations derived for larger magnitude data remain applicable for  $M < M_1$ . Plots similar to Figure 14 for the  $D_{5-75}$  and  $D_{5-95}$  duration parameters are given in Figures A10 and A11 in online Appendix A.

## STANDARD DEVIATION

The standard deviation model has two components: between-event standard deviation ( $\tau$ ) and within-event standard deviation ( $\phi$ ). Figure 15 shows binned values of both  $\tau$  and  $\phi$  with  $M$  and  $\phi$  with  $R_{rup}$  for  $D_{20-80}$  (results for other durations are in Figures A12 and A13 in the appendix). These standard deviations were derived using the full data set (including  $M < M_1$  events). Key features from these plots are that the  $\phi$  term is larger, and that while both terms are  $M$ -dependent, the sensitivity to  $M$  is greater for  $\phi$  than for  $\tau$ . Given the magnitude dependence of  $\phi$ , the trends of  $\phi$  versus  $R_{rup}$  were evaluated using data from events with  $M > 5.75$ , as shown in Figure 15c. Unlike with amplitude parameters (Boore et al. 2014), standard deviation,  $\phi$ , has no clear dependence on  $R_{rup}$ . We capture the  $M$ -dependence of  $\tau$  and  $\phi$  by computing standard deviations within relatively broad  $M$  bins (defined per Equations 14 and 15). We considered many possible limiting magnitudes for the upper bound of the low- $M$  bin and the lower bound of the high- $M$  bin. The bounding magnitudes reflected in Equations 14 and 15 reflect limits beyond which systematic changes in these standard deviations were not observed from these analyses. We use a simple linear interpolation between the limiting magnitudes, as shown in Figure 15.

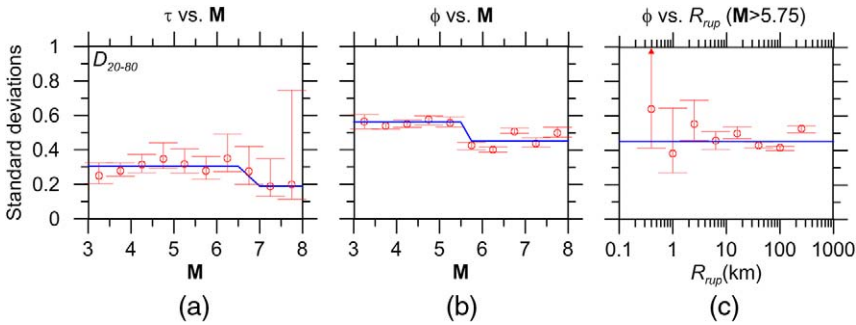


**Figure 15.** Binned standard deviation terms for  $D_{20-80}$  plotted against independent variables along with standard deviation models per Equations 14 and 15: (a) between-event standard deviation  $\tau$  vs. magnitude, (b) within-event standard deviation  $\phi$  vs. magnitude, and (c)  $\phi$  vs. distance for  $M > 5.75$  data. Confidence intervals for binned standard deviations are assumed to follow the chi distribution, which is not symmetric.

## COMPARISON TO PRIOR WORK

We compare the present model to the other recent duration GMPEs referenced in the *Introduction*. Separate comparisons are made for source, path, and total durations and we comment on epistemic uncertainties as inferred from these comparisons.

### SOURCE DURATION

Source durations are computed from the GMPEs using zero distance, a reference site condition of  $V_{S30} = 760$  m/s, and a strike-slip focal mechanism. Resulting trends of median  $D_{5-75}$  and  $D_{5-95}$  source durations with  $M$  are shown in Figure 16. Bearing in mind that the ordinate axis has a logarithmic scale, the ratio of upper/lower bound median models near the middle of the data range (around  $M$  6) is approximately a factor of 1.5 for  $D_{5-75}$  and two for  $D_{5-95}$ . This level of epistemic uncertainty almost certainly increases considerably beyond the approximate limits of the prior models, namely for  $M < 4 - 5$  and  $M > \sim 7.5$ . In both cases, our model deviates in its trends with  $M$  from extrapolations of prior models in the literature.

For  $D_{5-75}$ , all source models have an exponential form resulting in linear trends in semi-logarithmic space (as plotted, KS06 appears as slightly nonlinear due to an additive site term that is non-zero for  $V_{S30} = 760$  m/s). Our model also has an exponential form for source duration, but the tri-linear function for  $\Delta\sigma$  introduces slope changes at  $M_1$  and  $M_2$ . Our gradient expressing the scaling of source duration with  $M$  for  $M_1 < M < M_2$  is somewhat flatter than prior models, but is steeper for  $M > M_2$ . We note here that the prior models generally did not use data from the two  $M7.9$  events in the NGA-West2 data set (the exception is [Bommer et al. 2009](#), who used the NGA-West1 data set, which included the 2004 Alaska earthquake recordings), hence the present results are presumably better constrained at large magnitude. Results for  $D_{5-95}$  are similar, except that [Lee and Green \(2014\)](#) use a non-linear-exponential source function that produces a nonlinear trend in semi-logarithmic space

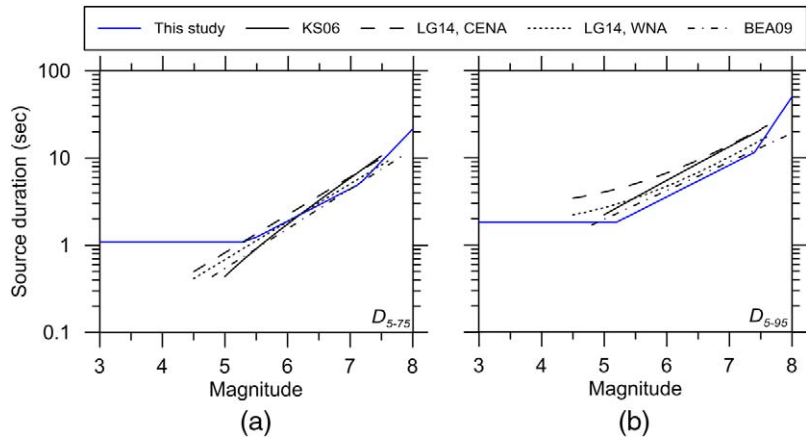


**Figure 16.** Comparison of the prediction by different models for zero distance and reference site condition ( $V_{S30} = 760$  m/s) for (a)  $D_{5-75}$  and (b)  $D_{5-95}$ . CENA = central and eastern North America; WNA = western North America; KS06 = [Kempton and Stewart \(2006\)](#); LG14 = [Lee and Green \(2014\)](#); BEA09 = [Bommer et al. \(2009\)](#).

(Figure 16). That nonlinear trend flattens at small  $M$ , approaching the constant source duration term employed in our model for  $M < M_1$ .

**PATH DURATION**

Our path duration term is additive, and as such can only be compared to similarly formatted additive path duration models in the literature (KS06; BT14). As shown in Figure 17, the path durations for different models have general similarity, although KS06 use a single slope and BT14 use a multilinear model with somewhat different trends than those found here (i.e., flatter between 40 and 120 km).

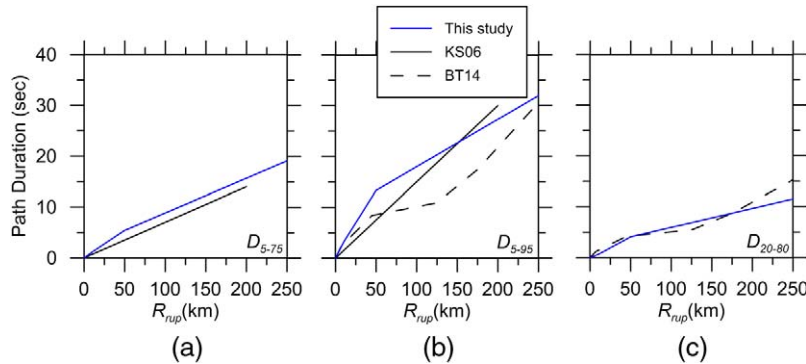


**Figure 17.** Comparison of path duration predicted by different models.

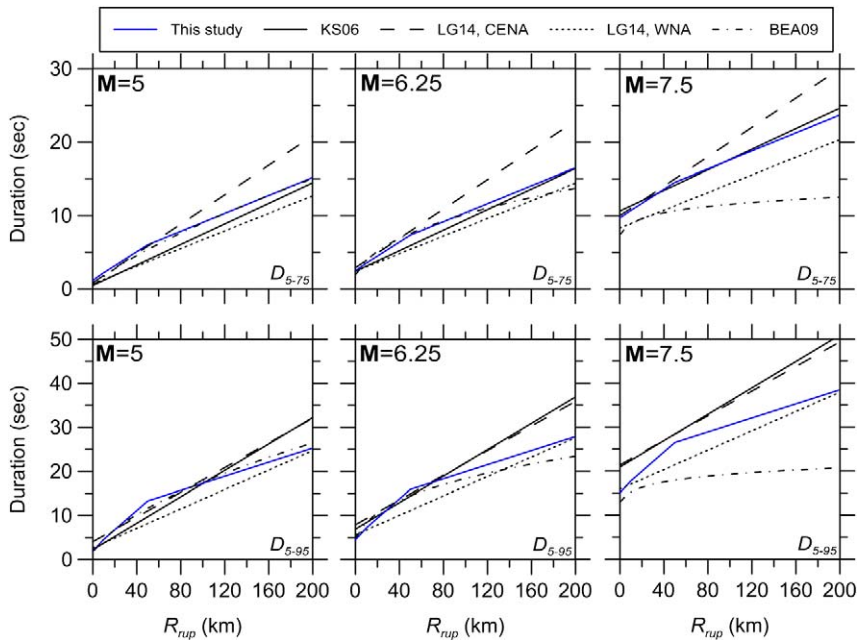


**Figure 18.** Comparisons of median durations predicted by recent models for a reference site condition ( $V_{S30} = 760$  m/s) and the duration parameters of  $D_{5-75}$  and  $D_{5-95}$ .

## TOTAL DURATION

We compare in Figure 18 total median durations predicted by our model with those for other recent duration GMPEs. We include each of the GMPEs discussed in the *Introduction* with the exception of Bora et al. (2014), which is not for significant duration. The source durations (at  $R_{rup} = 0$ ) exhibit model-to-model variability (largest/smallest) of about a factor of 1.5 for  $M \geq 6.25$ , which grows to a factor of more than two at a distance of 200 km.

The results in Figure 18 provide a more complete picture of model-to-model variability inclusive of path duration, because the use of total duration allows models with multiplicative path duration functions to be included. The variability is somewhat higher than is reflected in Figure 17, which is driven in part by the LG14 CENA model (which often provides upper bounds at large magnitudes) and the BEA09 model. The BEA09 model has a much flatter trend with distance at large magnitudes, which results from their use of an  $M$ -dependent path term in which path scaling decreases with  $M$ .

## CONCLUSIONS

We present GMPEs for three significant duration parameters derived from the NGA-West2 database. The new relations are a significant improvement over KS06 and other recent duration GMPEs because of the size of the database and associated improvements in the reliability of the models.



Our GMPEs are intended for application in tectonically active crustal regions. We recommend the following limits for the predictor variables used in our GMPEs:

- Strike-slip and reverse-slip earthquakes,  $M = 3$  to 8.0. As discussed in the text, epistemic uncertainties are relatively large below  $M$  5 (due to difficulties in separating source and path durations) and above  $M$  7.5 (due to only two events).
- Normal-slip earthquakes,  $M = 3$  to 7
- Distance,  $R_{rup} = 0$  km to 300 km
- Time-averaged shear wave velocities of  $V_{s30} = 150$  to 1,500 m/s
- Basin depth,  $z_1 = 0$  to 3.0 km
- CL1 (main shock) or CL2 (aftershock) event types

These limits are subjective estimates based on the distributions of the recordings used to develop the equations. Unlike KS06, we have not considered near-fault effects (such as pulse-like ground motions) in our formulation of the duration model. This was done in large part because of the lack of consensus from the NGA-West2 project on optimal parameterizations of near-fault effects. We expect these effects to be considered in future work.

## ACKNOWLEDGMENTS

The data set employed in this work was developed in the NGA-West2 project coordinated by the Pacific Earthquake Engineering Research (PEER) Center. We thank PEER, and in particular, Timothy Ancheta, Yousef Bozorgnia, Robert Darragh, and Tadahiro Kishida, for their invaluable roles in developing the data resources used in this study. This work was funded by the Southern California Earthquake Center (SCEC) and the National Science Foundation through SCEC award number 36558820. This support is gratefully acknowledged. Any opinions, findings, and conclusions or recommendations expressed in this material are those of the authors and do not necessarily reflect those of the National Science Foundation. We also thank Julian Bommer, David M. Boore, Jongwon Lee, and one anonymous reviewer for their helpful comments and suggestions.

## APPENDIX

Please refer to the online version of this paper to access the supplementary material provided in the Appendix.

## REFERENCES

- Abrahamson, N. A., and Silva, W. J., 1996. *Empirical Ground Motion Models*, Report to Brookhaven National Laboratory.
- Akkar, S., Sandikkaya, M. A., enyurt, M., Azari Sisi, A., Ay, B. Ö., Traversa, P., Douglas, J., Cotton, F., Luzi, L., Hernandez, B., and Godey, S., 2014. Reference database for seismic ground-motion in Europe (RESORCE), *Bull. Earthquake Eng.* **12**, 311–339.
- Allman, B., and Shearer, P., 2007. Spatial and temporal stress drop variations in small earthquakes near Parkfield, California, *J. Geophysical Res.* **112**, doi: 10.1029/2006JB004395.
- Allman, B., and Shearer, P., 2009. Global variations of stress drop for moderate to large earthquakes, *J. Geophysical Res.* **114**, doi: 10.1029/2008JB005821.

- Ancheta, T. D., Darragh, R. B., Stewart, J. P., Seyhan, E., Silva, W. J., Chiou, B. S.-J., Wooddell, K. E., Kottke, A. R., Boore, D. M., Kishida, T., and Donahue, J. L., 2014. NGA-West2 database, *Earthquake Spectra* **30**, 989–1005.
- Atkinson, G. M., and Beresnev, I., 1997. Don't call it stress drop, *Seism. Res. Letters* **68**, 3–4.
- Bommer, J. J., Stafford, P. J., and Alarcón, J. E., 2009. Empirical equations for the prediction of the significant, Bracketed, and uniform duration of earthquake ground motion, *Bull. Seism. Soc. Am.* **99**, 3217–3233.
- Boore, D. M., 2003. Simulation of ground motion using the stochastic method, *Pure and Applied Geophysics* **160**, 635–675.
- Boore, D. M., 2005. SMSIM—Fortran Programs for Simulating Ground Motions from Earthquakes: Version 2.3—A Revision of OFR 96- 80-A, Open-File Rpt. 00-509, U.S. Geological Survey, revised 15 August 2005, 55 pp.
- Boore, D. M., Stewart, J. P., Seyhan, E., and Atkinson, G. M., 2013. *NGA-West2 Equations for Predicting Response Spectral Accelerations for Shallow Crustal Earthquakes*, PEER Report No. 2013/05, Pacific Earthquake Engineering Research Center, University of California, Berkeley.
- Boore, D. M., Stewart, J. P., Seyhan, E., and Atkinson, G. M., 2014. NGA-West2 equations for predicting PGA, PGV, and 5%-damped PSA for shallow crustal earthquakes, *Earthquake Spectra* **30**, 1057–1085.
- Boore, D. M., and Thompson, E. M., 2014. Path durations for use in the stochastic-method simulation of ground motions, *Bull. Seism. Soc. Am.* **104**, 2541–2552.
- Bora, S. S., Scherbaum, F., Kuehn, N., and Stafford, P., 2014. Fourier spectral- and duration models for the generation of response spectra adjustable to different source-, propagation-, and site conditions, *Bull. Earthquake Eng.* **12**, 467–493.
- Bradley, B. A., 2011. Correlation of significant duration with amplitude and cumulative intensity measures and its use in ground motion selection, *J. Earthquake Eng.* **15**, 809–832.
- Bray, J. D., and Rathje, E. R., 1998. Earthquake-induced displacements of solid-waste landfills, *J. Geotech. & Geoenviron. Eng.* **124**, 242–253.
- Brune, J. N., 1970. Tectonic stress and the spectra of seismic shear waves from earthquakes, *J. Geophys. Res.* **75**, 4997–5009.
- Brune, J. N., 1971. Seismic sources, fault plane studies and tectonics, *EOS*. **52**, 178–187.
- Chandramohan, R., Baker, J. W., and Deierlein, G. G., 2016. Quantifying the influence of ground motion duration on structural collapse capacity using spectrally equivalent records, *Earthquake Spectra* **32**, 927–950.
- Chiou, B. S.-J., Darragh, R. B., Gregor, N., and Silva, W. J., 2008. NGA project strong-motion database, *Earthquake Spectra* **24**, 23–44.
- Cook, R. D., and Weisberg, S., 1999. *Applied Regression Including Computing and Graphics*, Wiley & Sons, Hoboken, NJ.
- Frankel, A. D., Stephenson, W. J., Carver, D. L., Williams, R. A., Odum, J. K., and Rhea, S., 2007. *Seismic Hazard Maps for Seattle, Washington, Incorporating 3D Sedimentary Basin Effects, Nonlinear Site Response, and Rupture Directivity*, USGS Open-File Report 2007-1175, 77 pp.
- Hancock, J., and Bommer, J. J., 2007. Using spectral matched records to explore the influence of strong-motion duration on inelastic structural response, *Soil Dyn. Earthquake Eng.* **27**, 291–299.

- Hanks, T. C., and Kanamori, H., 1979. A moment magnitude scale, *J. Geophys. Res.* **84**, 2348–2350.
- Hanks, T. C., and McGuire, R. K., 1981. The character of high-frequency strong ground motion, *Bull. Seismol. Soc. Am.* **71**, 2071–2095.
- Kempton, J. J., and Stewart, J. P., 2006. Prediction equations for significant duration of earthquake ground motions considering site and near-source effects, *Earthquake Spectra* **22**, 985–1013.
- Lee, J., and Green, R. A., 2014. An empirical significant duration relationship for stable continental regions, *Bull. Earthquake Eng.* **12**, 217–235.
- McGuire, R. K., Silva, W. J., and Costantino, C. J., 2001. *Technical Basis for Revision of Regulatory Guidance on Design Ground Motions: Hazard- and Risk-Consistent Ground Motion Spectra Guidelines*, NRC, Washington, D.C.
- Pearson, K., 1900. On the criterion that a given system of deviations from the probable in the case of a correlated system of variables is such that it can be reasonably supposed to have arisen from random sampling, *Philosophical Magazine* **50**, 157–175, doi:10.1080/14786440009463897.
- Pinheiro, H., Bates, D., DebRoy, S., and Sarkar, D., and the R Development Core Team, 2013. NLME: Linear and Nonlinear Mixed Effects Models, R package version 3.1–108.
- Raghunandan, M., and Liel, A. B., 2013. Effect of ground motion duration on earthquake-induced structural collapse, *Structural Safety* **41**, 119–133.
- Rezaeian, S., Bozorgnia, Y., Idriss, I. M., Abrahamson, N., Campbell, K., and Silva, W., 2014a. Damping scaling factors for elastic response spectra for shallow crustal earthquakes in active tectonic regions, *Earthquake Spectra* **30**, 939–963.
- Rezaeian, S., Bozorgnia, Y., Idriss, I. M., Abrahamson, N., Campbell, K., and Silva, W., 2014b. Damping scaling factors for vertical elastic response spectra for shallow crustal earthquakes in active tectonic regions, *Earthquake Spectra* **30**, 1335–1358.
- Seyhan, E., and Stewart, J. P., 2014. Semi-empirical nonlinear site amplification from NGA-West 2 data and simulations, *Earthquake Spectra* **30**, 1241–1256.
- Seyhan, E., Stewart, J. P., Ancheta, T. D., Darragh, R. B., and Graves, R. W., 2014. NGA-West 2 site database, *Earthquake Spectra* **30**, 1007–1024.
- Stafford, P. J., Mendis, R., and Bommer, J. J., 2008. The dependence of spectral damping ratios on duration and number of cycles. *J. Structural Eng.* **134**, 1364–1373.
- Trifunac, M. D., and Brady, A. G., 1975. A study on duration of strong earthquake ground motion, *Bull. Seismol. Soc. Am.* **65**, 581–626.
- Wang, C.-Y., Lee, Y.-H., Ger, M.-L., and Chen, Y.-L., 2004. Investigating Subsurface Structures and P- and S-wave Velocities in the Taipei Basin, *Terrestrial, Atmospheric and Oceanic Sciences (TAO)* **15**, 609–627.
- Wooddell, K. E., and Abrahamson, N. A., 2014. Classification of main shocks and aftershocks in the NGA-West 2 database, *Earthquake Spectra* **30**, 1257–1267.
- Zhang, S., Wang, G., Pang, B., and Du, C., 2013. The effects of strong motion duration on the dynamic response and accumulated damage of concrete gravity dams, *Soil Dyn. Earthquake Eng.* **45**, 112–124.

(Received 30 June 2015; accepted 7 February 2016)